Inertia–Gravity Waves Spontaneously Generated by Jets and Fronts. Part I: Different Baroclinic Life Cycles

RIWAL PLOUGONVEN*

School of Mathematics and Statistics, University of St Andrews, St Andrews, United Kingdom

CHRIS SNYDER

National Center for Atmospheric Research, Boulder, Colorado

(Manuscript received 9 June 2006, in final form 17 October 2006)

ABSTRACT

The spontaneous generation of inertia–gravity waves in idealized life cycles of baroclinic instability is investigated using the Weather Research and Forecasting Model. Two substantially different life cycles of baroclinic instability are obtained by varying the initial zonal jet. The wave generation depends strongly on the details of the baroclinic wave's development. In the life cycle dominated by cyclonic behavior, the most conspicuous gravity waves are excited by the upper-level jet and are broadly consistent with previous simulations of O'Sullivan and Dunkerton. In the life cycle that is dominated by anticyclonic behavior, the most conspicuous gravity waves even in the stratosphere are excited by the surface fronts, although the fronts are no stronger than in the cyclonic life cycle. The anticyclonic life cycle also reveals waves in the lower stratosphere above the upper-level trough of the baroclinic wave; these waves have not been previously identified in idealized simulations. The sensitivities of the different waves to both resolution and dissipation are discussed.

1. Introduction

The mechanisms responsible for the excitation of gravity waves from initially balanced motions remain poorly understood. A good starting point to investigate this problem consists in idealized baroclinic life cycles: these are realistic enough to allow direct comparison with observations, yet retain simplicity as we can perfectly control the initial conditions and exclude moist processes. Previous studies of gravity wave excitation in baroclinic life cycles (O'Sullivan and Dunkerton 1995; Zhang 2004) have emphasized at least two classes of waves being generated. These studies agree with evidence from observations [e.g., the key role of jet exit regions (Uccellini and Koch 1987)], but do not investigate other aspects, such as waves associated with upper-level troughs (Plougonven et al. 2003) or surface fronts (Eckermann and Vincent 1993). The latter have also been identified in numerical simulation of two-dimensional frontogenesis (Snyder et al. 1993).

In this paper, we also investigate gravity wave emission by idealized baroclinic waves. There is as yet no theory for wave emission directly applicable to this context and so we do not attempt a quantitative comparison of the simulations against theory. Instead, we document the various inertia–gravity waves appearing in multiple regions within the baroclinic wave, how those can change for different baroclinic life cycles and how they depend on numerical aspects of the simulations such as resolution and dissipation.

Improving our understanding of sources of gravity waves is motivated by the several roles of gravity waves in the atmosphere. At small scales, gravity waves can induce turbulence (e.g., Lane et al. 2004), influence chemistry when there is sensitivity to small temperature fluctuations (Shibata et al. 2003; Buss et al. 2004), and modulate severe weather (e.g., Stobie et al. 1983; Bosart and Sanders 1986). On the global scale the vertical transfers of momentum due to gravity waves are crucial to the circulation of the middle atmosphere (Fritts and Alexander 2003). At present, the main weakness of parameterizations of these waves in gen-

* Current affiliation: Laboratoire de Météorologie Dynamique, ENS, IPSL, Paris, France.

Corresponding author address: Riwal Plougonven, Laboratoire de Météorologie Dynamique, Ecole Normale Supérieure, 24 rue Lhomond, 75231 Paris CEDEX 05, France.
E-mail: riwal.plougonven@polytechnique.org

DOI: 10.1175/JAS3953.1

eral circulation models is the largely arbitrary description of the sources (Kim et al. 2003; McLandress and Scinocca 2005), in particular jet/front systems. Attempts to parameterize jet/front systems as sources remain limited owing to our lack of understanding of the generation mechanisms (Charron and Manzini 2002).

Previous studies of gravity waves excited by jets and fronts follow three lines of investigation. The first is studies based on observations, which have often emphasized the jet exit region upstream of a ridge as a key region of intense gravity wave activity (Uccellini and Koch 1987; Guest et al. 2000; Pavelin et al. 2001). Intense, low-frequency gravity waves have also been observed in jet exit regions upstream of an upper-level trough (Plougonven et al. 2003). Plougonven et al. (2003), as well as Thomas et al. (1999), noted gravity wave packets propagating upward in the lower stratosphere and downward in the midtroposphere, indicating that the jet was the likely source. Other observations have highlighted surface fronts as important sources of gravity waves (Fritts and Nastrom 1992; Eckermann and Vincent 1993), though they have the complication of including wave emission by the balanced motions as well as other possible sources, such as deep convection along the front.

The second line of investigation is numerical studies of two-dimensional frontogenesis. Snyder et al. (1993) and Griffiths and Reeder (1996) showed that fronts can be significant sources of gravity waves. In those simulations, the wave emission becomes more pronounced as the frontal scale contracts (Snyder et al. 1993) or when the frontogenesis varies rapidly (Reeder and Griffiths 1996). Though idealized, the simulations also demonstrated the importance of numerical considerations in wave-emission studies by showing that spurious gravity waves were produced when resolution was insufficient (Snyder et al. 1993).

The third is numerical studies of idealized three-dimensional baroclinic instability. O'Sullivan and Dunkerton (1995) simulated baroclinic waves on the sphere and found that inertia–gravity waves with near-inertial frequencies appeared in the stratosphere above and just downstream from the upper-level ridge. Zhang (2004) considered baroclinic waves in a channel on the f plane. He identified a second class of waves in the stratosphere, above a jet-exit region near the ridge axis and of shorter wavelength and higher frequency than the waves found by O'Sullivan and Dunkerton.

The gravity waves associated with both fronts and jets in the aforementioned studies potentially arise from wave emission by the larger-scale, balanced flow (this has been called spontaneous emission or Lighthill radiation; cf. Ford et al. 2000). This radiation can be described theoretically for the emission of large-scale gravity waves from small-scale balanced motions (Ford 1994; Ford et al. 2000; Plougonven and Zeitlin 2002). In the case of small Rossby numbers and for gravity waves having scales similar to those of the balanced motions, a classical weakly nonlinear approach does not reveal any emission of gravity waves (e.g., Reznik et al. 2001). Only for some specific flows (constant horizontal or vertical shear) have mechanisms of coupling between gravity waves and balanced motions at small Rossby number been theoretically described (Vanneste and Yavneh 2004; Plougonven et al. 2005; Molemaker et al. 2005), and this coupling was found to be exponentially small in Rossby number.

As yet, the above theoretical investigations do not provide a quantitative prediction of the gravity waves to be excited by baroclinic waves. In this context, geostrophic adjustment has often been invoked (O'Sullivan and Dunkerton 1995; Zhang 2004; Pavelin et al. 2001) to explain qualitatively the generation of the waves from jets, but here again, theoretical studies are constrained to situations that are too idealized (e.g., Fritts and Luo 1992; Plougonven and Zeitlin 2005) to provide quantitative predictions in flows that are time-dependent and spatially complex, and where the imbalance is not a given initial condition but is continuously forced and ambiguously defined. Hence, in the present paper we will not yet attempt to quantitatively explain the excited gravity waves but simply, as a first step, describe them and identify the regions generating them.

To bring together the various threads outlined above, we use the Weather Research and Forecasting Model (WRF; see Skamarock et al. 2005) to simulate different baroclinic life cycles (section 2). The gravity waves appearing in a standard life cycle, dominated by cyclonic behavior (section 3), differ markedly with those appearing in an anticyclonic life cycle (section 4). They nevertheless have in common their ground-based phase speed (section 5). Crucial numerical issues, in particular sensitivity to resolution and dissipation, are discussed in section 6. Results and directions for further investigation are summarized in 7.

2. Experimental setup

The numerical simulations employ the Advanced Research dynamical core of the WRF model (Skamarock et al. 2005), which solves the compressible, nonhydrostatic equations of fluid motion. We assume the flow is confined to a periodic channel on the f plane, with period 4000 km in the zonal (x) direction and walls separated by 10 000 km in the meridional (y) direction.

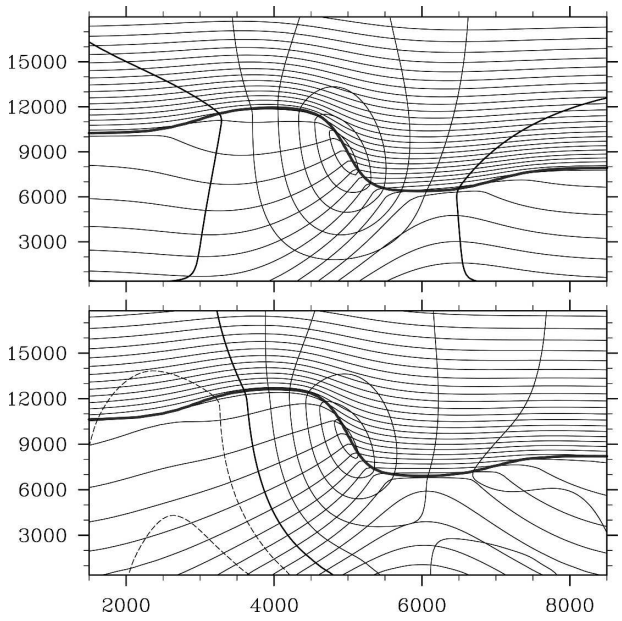

FIG. 1. Meridional cross sections of the initial balanced jets used in the two experiments. Horizontal axis is the meridional coordinate y in km; vertical axis is altitude z in m. The lines show the potential temperature (contours every 5 K), and the zonal velocity (contours every 10 m s^{-1}; the zero contour is thicker and negative contours are dashed). Also indicated as a thick gray line is the tropopause (3 PVU).

To study the spontaneous generation of inertia–gravity waves, the initial fields must be as unambiguously free of gravity waves as possible. The initial conditions are taken as a superposition of a geostrophically balanced zonal jet and its most unstable normal mode having a 4000-km zonal wavelength. The first life cycle exhibits predominantly cyclonic behavior. To obtain a second life cycle with a predominant anticyclonic behavior, we add a strong anticyclonic shear ($0.18f$) at the surface to the zonal jet (cf. appendix A).

The initial jets are shown in Fig. 1. They are obtained by inverting two-dimensional potential vorticity (PV) distributions in the y–z plane, prescribed in a way similar to that of Rotunno et al. (1994): a troposphere with uniform PV of 0.4 potential vorticity units (PVU; 1 PVU = 10^{-6} m^{-2} s^{-1} K kg^{-1}), separated by a sharp tropopause from a stratosphere with uniform PV of 4 PVU (see appendix A). When used as initial conditions, these jets undergo a small adjustment. To eliminate this, all fields were time-averaged over two inertial periods. The obtained fields defined a new initial condition, and the process was repeated twice, so that the initial adjustment is reduced to oscillations that are less than 10^{-3} m s^{-1} in horizontal wind.

The most unstable mode with 4000-km wavelength is computed by evolving a small perturbation to the jet for 4 days, then rescaling the perturbation to a smaller amplitude and starting the cycle again. After 16 total days of integration, the normal mode is extracted, rescaled so that its maximum perturbation in potential temperature is 0.1 K and added to the zonal jet.

The resolution used, unless indicated otherwise, was $dx = 50$ km and $dz = 250$ m (reference). Lower ($dx = 100$ km, $dz = 500$ m) and higher resolution ($dx = 25$ km, $dz = 125$ m) runs were made to test the sensitivity of results to resolution and will be discussed in section 6. The vertical resolution was always chosen so that $dx/dz = 200$.

The simulations include explicit numerical dissipation in order to avoid the development of spurious structures at the smallest scales of the flow, in particular near the surface fronts. Several different forms of dissipation were tested. The scheme retained for the simulations presented here consisted in a fourth-order hyper-diffusion multiplied by a spatially varying coefficient that was proportional to the deformation of the flow where the deformation was weaker than $2f$, and constant where deformation exceeded that value. For the reference runs ($\Delta x = 50$ km), the maximum diffusivity was -2.75×10^{14} m^4 s^{-1}. The proportionality constant was set so that the dissipation coefficient was continuous (e.g., -1.375×10^{18} m^4 in the reference runs). For lower or higher resolution, the maximum value of diffusivity was adequately multiplied or divided so that $\nu\, dt/dx^4$ remained constant. The sensitivity of our experiments to the choice of the dissipation scheme will be discussed in section 6.

3. Gravity waves generated in a standard baroclinic life cycle

In the standard life cycle (see Figs. 1 and 2), the development of the baroclinic wave is dominated by a cyclonic behavior (LC2 in the terminology of Thorncroft et al., 1993), which is typical of baroclinic instability in Cartesian geometry (Polavarapu and Peltier 1990; Snyder et al. 1991).

a. Inertia–gravity waves along the jet, from ridge to trough

The most conspicuous inertia–gravity wave packet appearing in this simulation appears along the jet, from the ridge to the trough. This packet is clearest in the lower stratosphere propagating upward, but it also has a counterpart propagating downward from the jet in the troposphere.

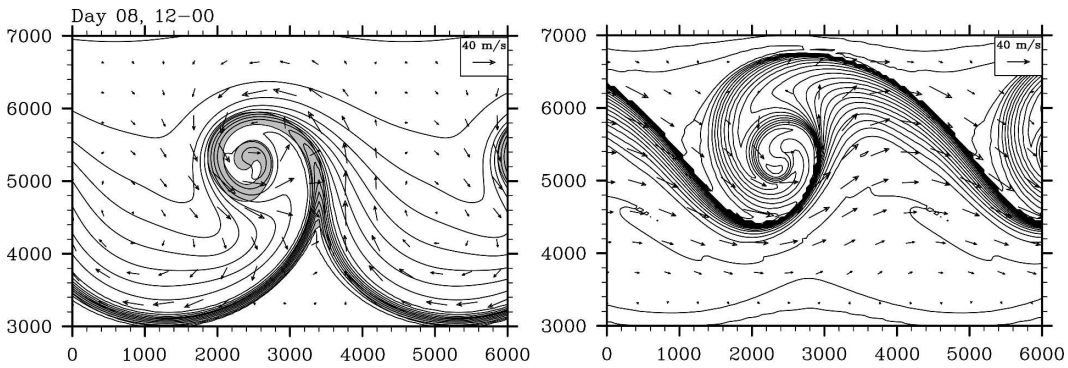

FIG. 2. Maps of the potential temperature (contours every 2 K) (left) at $z=150$ m and (right) on the tropopause (taken as the 3-PVU surface) showing the cyclonic development of the standard life cycle, at day 8, 1200 UTC. The shaded region in the left panel indicates regions where the relative vorticity exceeds $1.25f$, where $f=10^{-4}$ s^{-1} is the Coriolis parameter.

The location and orientation of the inertia–gravity waves appearing in the lower stratosphere are shown in Fig. 3. The waves appear just above the core of the jet, in the region of strong vertical shear near the tropopause, on the eastern side of the ridge of geopotential. In the horizontal, the phase lines are oriented from northwest to southeast, and are nearly parallel to the tropopause and the upper-level front.

The characteristics of the waves were determined by finding the sinusoidal wave packet that best correlated with the variations of the divergence or of the vertical velocity (see appendix B). The characteristics of the waves obtained from this analysis at day 8.5 of the simulation are listed in Table 1. From these, the dispersion relation (e.g., Gill 1982) provides a first estimate of the intrinsic frequency $\tilde{\omega}$:

$$\tilde{\omega}^2 = \frac{f^2m^2 + N^2(k^2 + l^2)}{k^2 + l^2 + m^2}, \qquad (1)$$

where (k, l, m) are the wavenumbers, f is the Coriolis parameter, and N is the Brunt–Väisälä frequency. The waves are found to be near-inertial, with a frequency of about $1.3f$.

Another estimate of the frequency can be obtained, independently, by analyzing Eulerian time series of $\nabla \cdot \mathbf{u}_H$ at one point in space. For the example shown in Fig. 4, the absolute frequency, ω_a, is about $2\pi/(7\text{ h})$. The intrinsic frequency of the wave is then recovered from $\tilde{\omega} = \omega_a - \mathbf{k} \cdot \mathbf{U}$, where $\mathbf{U} \sim (37\text{ m s}^{-1}, -2\text{ m s}^{-1})$ is the background horizontal wind, yielding $\tilde{\omega} \sim 1.44f$. The consistency with our first estimate provides evidence that the feature is indeed a gravity wave.

Even wave packets that are clearly defined (Fig. 3), have some spatial inhomogeneity, which leads to uncertainty in the packet's characteristics (see Table 1 and section 3b). In observational studies, this uncertainty will compound that arising from an incomplete knowledge of the flow (Zhang et al. 2004).

Investigation of the phase relations between the small-scale perturbations of the ageostrophic wind (see Fig. 5) brings further confirmation that the signal described above is indeed a gravity wave.[1] Moreover, the phase relations show that the waves above the jet are propagating upward, whereas the waves below the jet are propagating downward.

The zonal phase velocity relative to the ground can be calculated in several ways [intrinsic phase velocity plus the average background wind, directly from ω_a/k, of from Hovmöller diagrams (see section 5)], and is found to be about 15 m s^{-1}. Hence, given the wind velocities in the stratosphere (Fig. 1), the inertia–gravity waves generated above the jet are free to propagate upward, as they will not encounter a critical level.

Estimates of the group velocities from the values given in Table 1 yield $\mathbf{c}_g = (2.2, 2.0, 0.016)$ m s^{-1} for the simulation with 50-km resolution, corresponding to displacements over one day of roughly 190, 175, and 1.35 km in x, y, and z, respectively. In the simulations, the wave packet is indeed found to propagate upward into the stratosphere by approximately 3–5 km in two days (see Fig. 3 of Plougonven and Snyder 2005).

Finally, the waves are of moderate amplitudes: at the standard resolution, the maximum perturbation divergence due to the wave signal is found to be of order 0.15–$0.2f$ (see Table 4). In horizontal and vertical velocity, they were found to have signatures of the order

[1] The small-scale part of different fields was obtained by removing a smoothed version of the field. The smoothing was done by running averages, averaging values in cubes around each point.

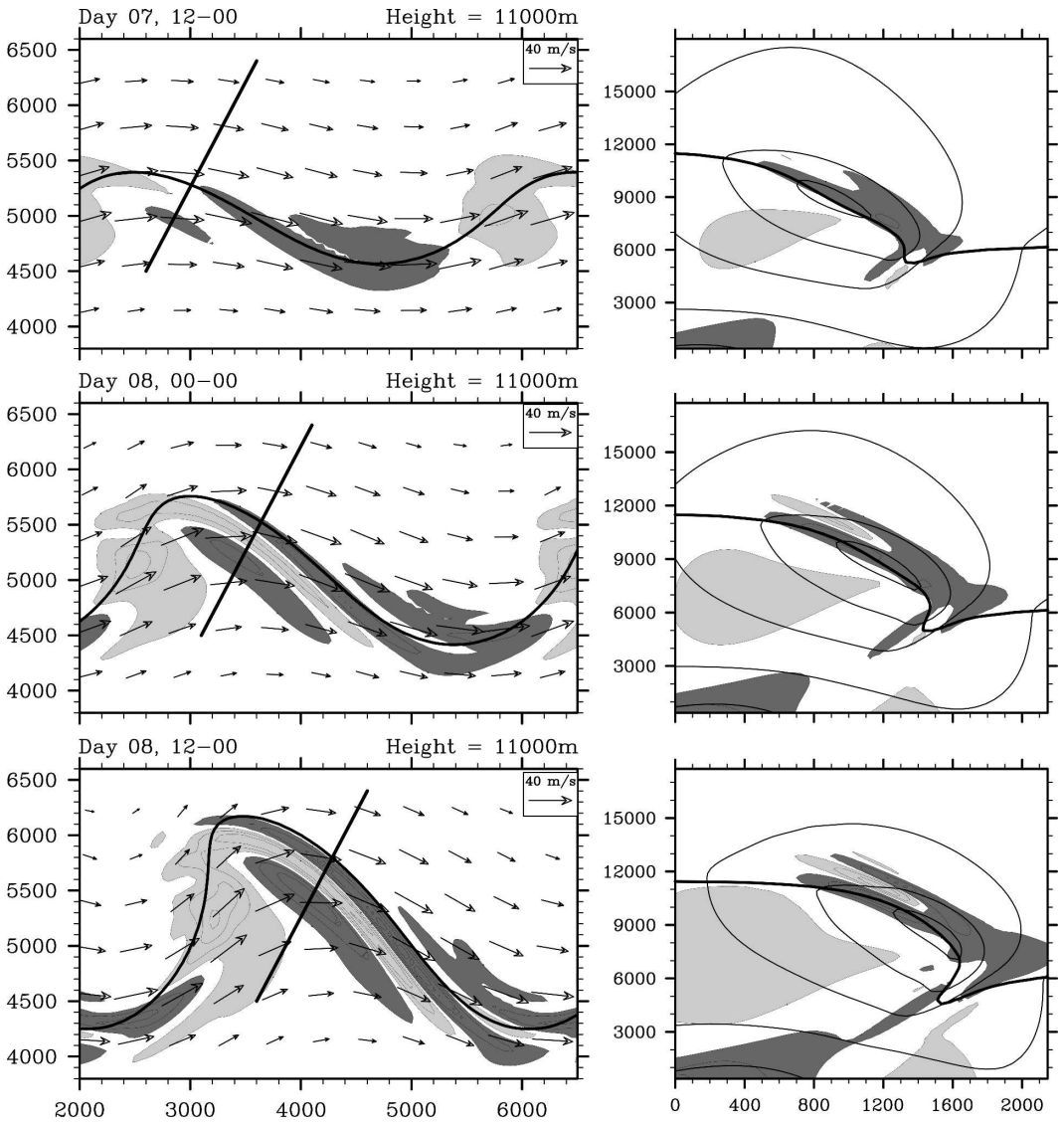

FIG. 3. Inertia–gravity waves appearing in the vicinity of the jet stream: (left) horizontal maps (at $z = 11$ km) of $\nabla \cdot \mathbf{u}_H$ (contours are every $0.08f$, with the values closest to 0 being $-0.04f$ and $0.04f$; dark gray for values lower than $-0.04f$, light gray for values larger than $0.04f$) and wind. The thick curve indicates the location of the tropopause (3 PVU) at $z = 9$ km. (right) Cross sections taken from location given by line segment at left. The tropopause (3 PVU), $\nabla \cdot \mathbf{u}_H$ (same contours), and the velocity normal to the cross section (contours every 15 m s^{-1}) are shown.

TABLE 1. Characteristics (wavelengths in km, and intrinsic frequency scaled by f) of the inertia–gravity waves present above and below the flank of the jet stream in the standard life cycle. For each resolution, the first line gives the values for the waves above the jet stream, and the second for those below (section 3a).

Resolution	λ_x	λ_y	λ_h	λ_z	$\tilde{\omega}$ from dispersion relation
$\Delta x = 100$ km	735 ± 60	810 ± 40	545 ± 30	2.40 ± 0.2	1.25 ± 0.02
	770 ± 140	790 ± 155	550 ± 100	2.50 ± 0.15	1.17 ± 0.05
$\Delta x = 50$ km	475 ± 55	525 ± 70	350 ± 45	1.70 ± 0.2	1.29 ± 0.02
	520 ± 55	490 ± 50	355 ± 35	2.10 ± 0.15	1.26 ± 0.05
$\Delta x = 25$ km	305 ± 45	330 ± 50	225 ± 35	1.10 ± 0.1	1.30 ± 0.03
	285 ± 35	295 ± 40	205 ± 25	1.45 ± 0.25	1.33 ± 0.04

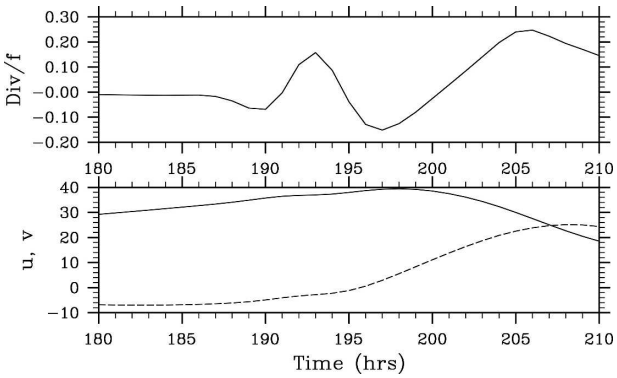

FIG. 4. Temporal evolution of (upper) the divergence and (lower) the horizontal wind at point (x = 500 km, y = 5500 km, z = 11 km) from the standard baroclinic life cycle. The horizontal axis shows the time in hours (180 h corresponds to 1200 UTC day 7, 210 h corresponds to 1800 UTC day 8).

of 1–1.2 m s^{-1} and 3–4 $\times$ 10^{-3} m s^{-1}, respectively. They are weaker than what has been observed in case studies of large inertia–gravity waves in the atmosphere (e.g., wind anomalies of up to 5–8 m s^{-1}). This is in part because we focus here on the early times when gravity waves appear in the flow and in part to the effects of the resolution and of the dissipation scheme (see Fig. 6 and section 6), but it is also possible that the waves described in observational case studies represent particularly intense examples of wave emission, and that other mechanisms combine with the dry mechanisms described in the present study to produce stronger gravity waves (e.g., Zhang et al. 2001).

The waves discussed in the present section are in several ways comparable with the ones discussed in O'Sullivan and Dunkerton (1995). In both cases the waves are low frequency (the ratio of the intrinsic frequency to the local value of f is 1.4–1.6 in O'Sullivan and Dunkerton's simulations). The wavelengths indicated in O'Sullivan and Dunkerton (1995) are comparable to the ones found in our low-resolution run (see Table 1). In both cases, the waves appear in a jet exit region in the highly sheared region just above the jet core. Their phase lines are nearly normal to the flow there. Nevertheless, the comparison cannot be developed further as the two baroclinic life cycles differ substantially.

In contrast to O'Sullivan and Dunkerton (1995), the inertia–gravity waves found here in the lower stratosphere have a tropospheric counterpart below the core of the jet (see vertical cross sections in Fig. 3 and right panel of Fig. 5) at altitudes between 4 and 8 km. Both wave packets appear in regions of strong vertical shear, with similar characteristics (see Table 1), but the waves below the jet have weaker amplitudes (Table 4) and have downward group velocity (Fig. 5). This is clear evidence that the upper-level jet is the source of these waves.

b. Stratospheric wave packet comparable to Zhang

Another inertia–gravity wave packet is found in the upper-troposphere, lower-stratosphere region, above the jet and on the northwest side of the ridge (Fig. 7. This wave packet is very similar to the mesoscale waves described by Zhang (2004) in idealized simulations of baroclinic instability using a similar initial jet, and we will call it the Zhang wave packet. Zhang described

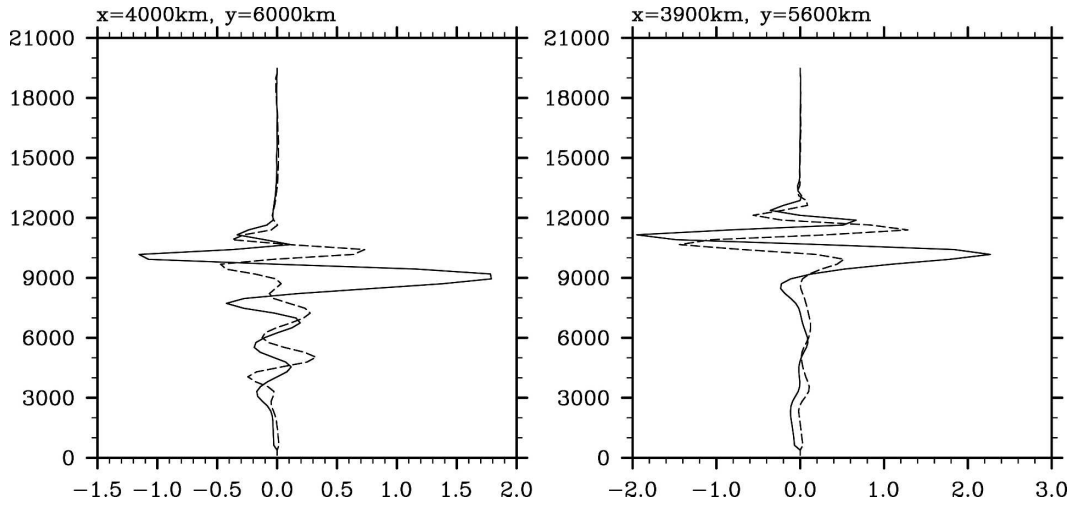

FIG. 5. Vertical profiles of the small-scale part to the ageostrophic wind (u' is solid line; v' is dashed line) at points (left) x = 4000 km and y = 6000 km and (right) x = 3900 km and y = 5600 km for 1200 UTC day 8 of the standard life cycle. The phase relations between the two velocity components indicate that the wave below the jet is propagating energy downward, whereas the wave above the jet is propagating energy upward.

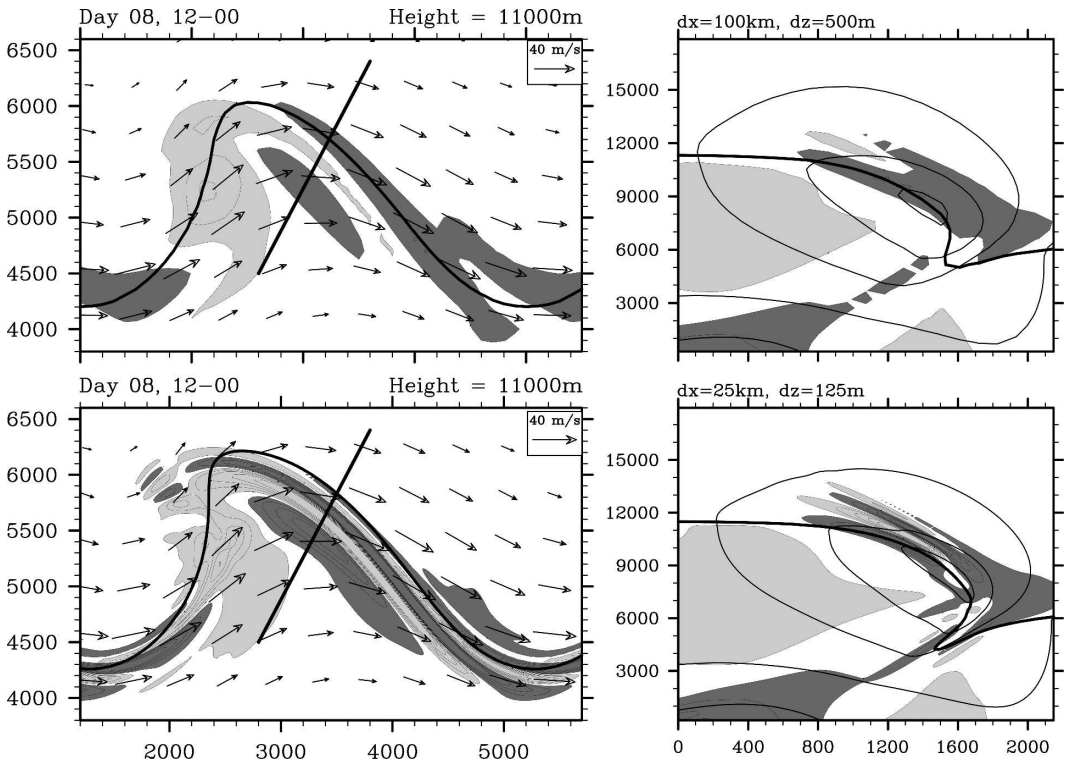

FIG. 6. (left) Horizontal and (right) vertical cross sections to be compared with those of the bottom row in Fig. 3 (standard life cycle, 1200 UTC day 8). The resolution is halved in the top panels and doubled in the bottom panels.

these waves as mesoscale to distinguish them from the longer-wavelength waves described by O'Sullivan and Dunkerton (1995). However, in our simulations the waves described in section 3a and those described in the present section have similar wavelengths and both belong to the mesoscale.

Figure 7 shows cross sections of the Zhang wave packet at the three resolutions used, in the same format as the one used by Zhang (2004) for his Figs. 4d and 6d. Although the models used are not the same and the synoptic-scale baroclinic system is periodic in our case and localized in Zhang's simulations, the signature of these waves is remarkably similar, which adds credibility to both sets of simulations. The amplitude of the divergence signal in our high-resolution run ($\Delta x = 25$ km, lower panel of Fig. 7) is very comparable to the one obtained in the domain with $\Delta x = 30$ km in Zhang (2004, his Fig. 4d).

The Zhang wave packet has a more complex spatial structure than the one described in section 3a. In the cross sections at $z = 13$ km (Fig. 7), the orientation of the phase lines in the region where the wave packet is most intense indicate a wave vector pointing between north and north–northeast. The phase lines connect to those of the wave packet described in section 3a. Yet at lower heights, there is clearly the signature of two distinct wave packets. At $z = 11$ cm, the smaller wave packet is seen in the lower panel of Fig. 6 to have a wave vector pointing to the northwest, and to have a very limited extent. At lower heights still (not shown), the smaller wave packet is oriented further toward the west. The two wave packets also differ in their sensitivity to resolution and dissipation, the Zhang wave packet being much more sensitive to both (see section 6 and Fig. 15).

Because of the complex spatial structure and the limited extent of this wave packet, its characteristics are more difficult to define. Horizontal and vertical wavelengths are determined visually to be about 300 and 3 km, respectively, in the reference simulation. In the high-resolution run, the corresponding wavelengths are 200 and 2 km (Fig. 7), comparable to the ones described by Zhang (2004). This yields, from the dispersion relation, an intrinsic frequency of about $2f$, and hence a higher vertical group velocity ($\sim$0.05 m s^{-1} or $\sim$4 km day^{-1}) than the wave packet described in section 3a.

The complex structure of this wave packet and its location make it difficult to identify a possible source.

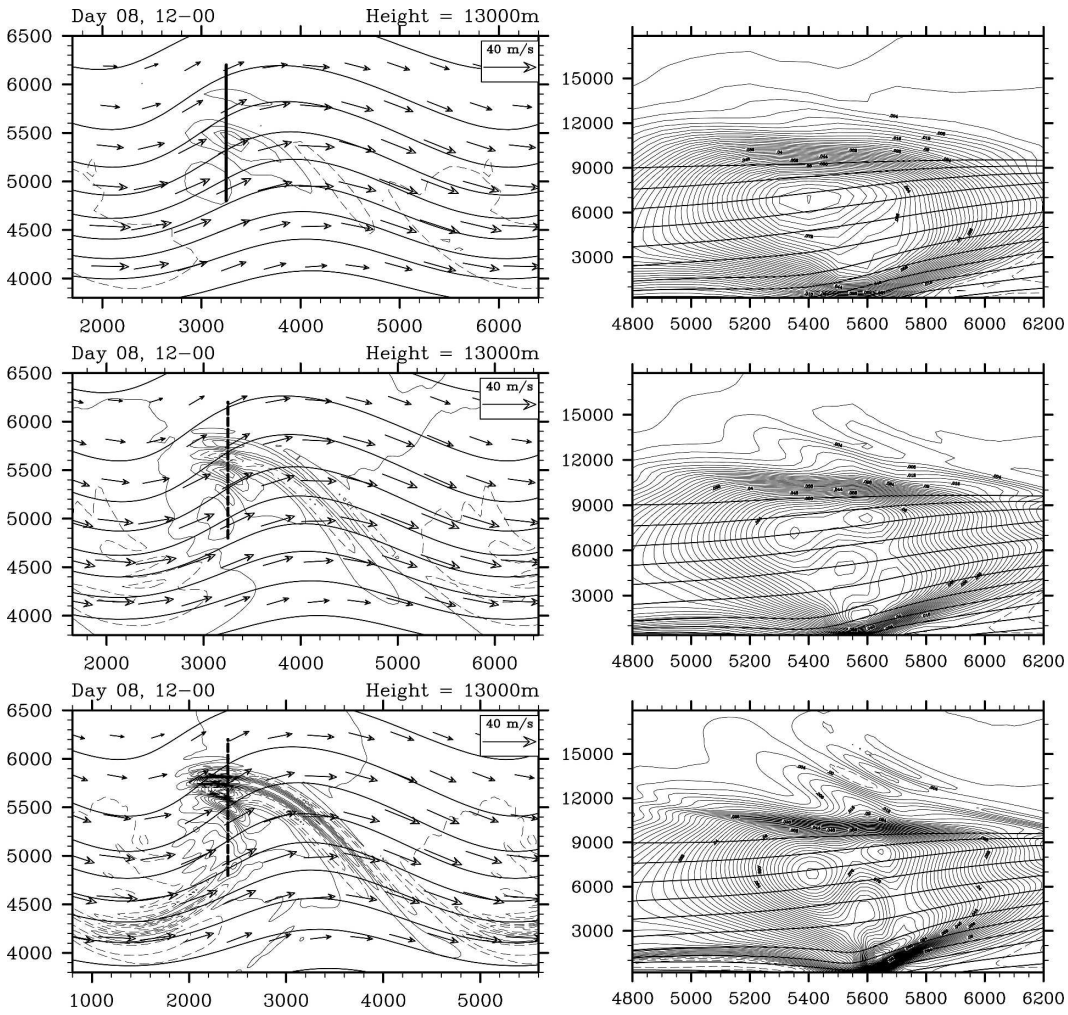

FIG. 7. (left) Horizontal and (right) vertical cross sections showing the wave packet similar to the one described by Zhang (2004), in the standard life cycle, at (top) low resolution (Δx = 100 km), (middle) moderate resolution (Δx = 50 km), and (bottom) high resolution (Δx = 25 km). The figures are made to be comparable to Figs. 4d and 6d of Zhang (2004). The horizontal cross sections are taken at z = 13 km. They show $\nabla \cdot \mathbf{u}_H$ (contour interval $0.02f$), and wind and pressure (contour interval is 2 hPa). The vertical cross sections show the vertical velocity (contour interval is 2×10^{-3} m s^{-1}), and tropospheric values of the potential temperature (contour interval is 5 K).

As can be seen from the vertical cross sections in Fig. 7, it appears above the occlusion, a region where the flow and trajectories are known to become small-scale and complex (Rotunno et al. 1994).

c. *Gravity waves associated with surface fronts*

Finally, we note that the simulations also contain indications of weak gravity waves above surface fronts, both warm and cold, as can be seen from Fig. 8. The waves are qualitatively comparable to the ones generated by surface fronts in idealized two-dimensional simulations (Snyder et al. 1993). Similar gravity waves excited from the surface fronts are much more intense and identifiable in the anticyclonic life cycle, presented below.

4. Gravity waves generated in an anticyclonic baroclinic life cycle

To confirm that surface fronts can be significant sources of inertia–gravity waves, a second baroclinic life cycle is presented below, in which waves generated by the surface fronts are the most conspicuous gravity wave signal present. The initial state for this different baroclinic life cycle exhibits strong anticyclonic shear in u at the surface (up to $0.18f$) and in the lower troposphere, see Fig. 1. The development of the baroclinic

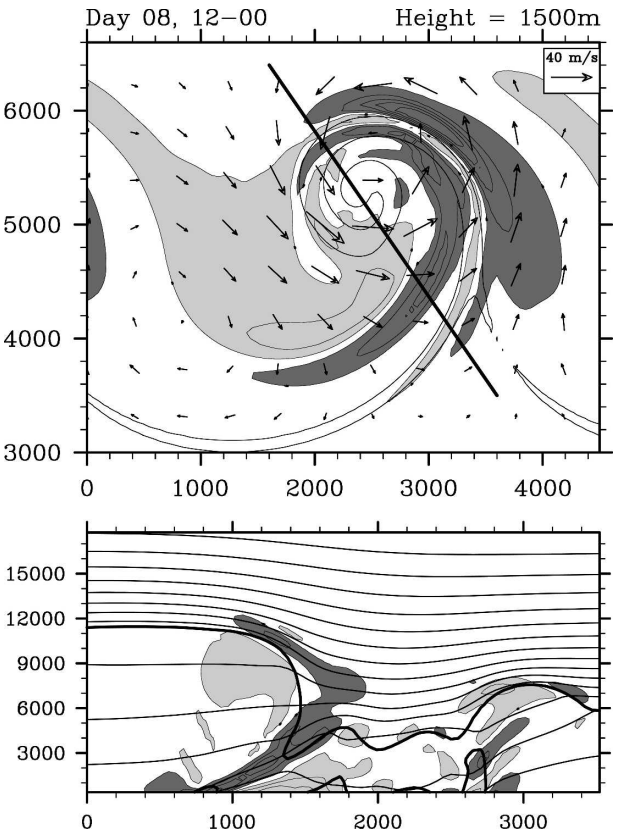

FIG. 8. Gravity waves associated to the warm and cold fronts for the standard life cycle, at 1200 UTC day 8. (top) Horizontal cross section of $\nabla \cdot \mathbf{u}_H$, wind at $z = 1500$ m. As a reminder of the location of the surface fronts below, a thin line indicates the contour where relative vorticity at $z = 150$ m is equal to $1.25f$. (bottom) Vertical cross section through the line indicated in the top panel. Contours as in Fig. 3, but the thin lines indicate the potential temperature (every 10 K) instead of the normal velocity.

instability is here dramatically different, as displayed in Fig. 9. A strong cold front develops at the surface, and advances southward into regions of surface easterly winds as the anticyclone that dominates the flow broadens.

a. Waves generated by the surface cold front

Inspection of the horizontal divergence field reveals that the most conspicuous wave signal in this case appears in the troposphere, just ahead of the cold front to the south (Fig. 10). The phase lines of the waves are essentially parallel to the cold front below. Again, phase relations and vertical cross sections show that these waves propagate upward and hence that the surface front is unambiguously the source.

The horizontal wavelengths (Table 2) are slightly shorter but comparable to those found in the vicinity of the upper-level jet in section 3a. On the other hand, their vertical wavelengths are much longer (5–6 km), yielding larger intrinsic frequencies (2–3f). This implies that these waves propagate upward much more rapidly, and this is easily seen in Fig. 10. The vertical group velocity of these waves estimated from the linear dispersion relation is 0.25 ± 0.03 m s^{-1}, which corresponds to roughly 10 km in 12 h, consistent with Fig. 10.

The zonal phase velocity relative to the ground was found to be about 14 ± 1 m s^{-1}. Again, this implies that the waves excited by the front are free to propagate upward, given the vertical distribution of winds in our simulation. As the waves are excited in a region of strong easterlies, their phase velocity relative to the wind is quite fast (about 24 ± 2 m s^{-1}). The waves have a signature in $\nabla \cdot \mathbf{u}_H$ of the order of 0.1–0.15f (see Table 4) in the reference simulation, which is comparable to the waves described in the standard life cycle.

Again, note that the notion of a wave packet is convenient but has limitations: the waves extend along the whole front, and their characteristics are spatially inhomogeneous. For instance, note how the phase lines follow the distortion of the surface front to the northeast in the high-resolution run (Fig. 11, vicinity of $x = 5000$ km, $y = 6400$ km).

It is likely that the generation mechanism here differs substantially from the one responsible for the waves excited by the jet in the standard run (section 3a). The latter had their phase lines roughly parallel to the tropopause or to the tropopause fold (Fig. 3). Here, the waves emanating from the surface fronts have their phase lines tilt in the direction opposite to the frontal region (Fig. 10), as in the 2D simulations of Snyder et al. (1993). Note also that this tilt is consistent with an interpretation of the waves as topographic waves excited in a sheared flow above an obstacle (Ralph et al. 1999). Zonal cross sections are suggestive of this interpretation (not shown). It would also be consistent with the fact that waves emanating from the surface fronts in the standard run were much weaker, and with the vertical wavelengths of the waves being rather insensitive to resolution [m being set by the background values for u and N, e.g., Gill (1982)]. Nevertheless, further work is needed to determine the relevance of this interpretation.

b. Waves in the tropopause region

In the lower stratosphere, two wave packets can be identified in the anticyclonic life cycle. The first is simply the one described in the previous section, propagating upward to the stratosphere where the winds allow (Figs. 12). The second, located farther north, is a smaller wave located above a deep tropopause fold. Its

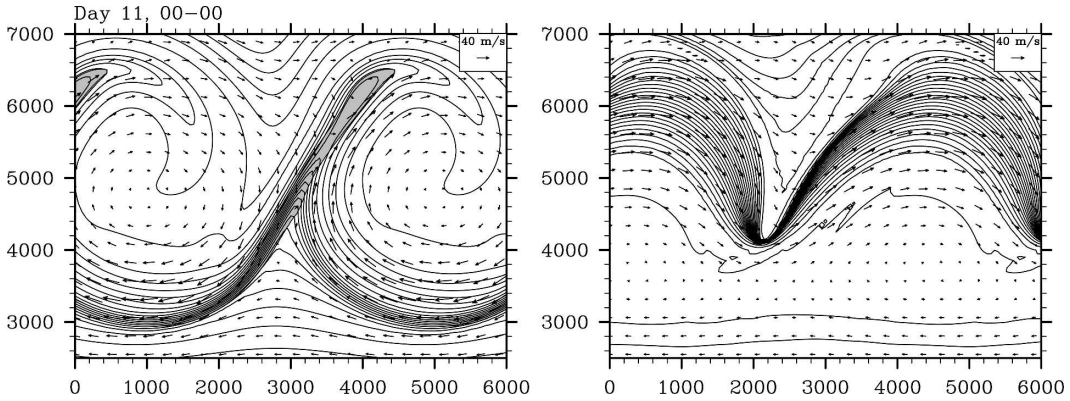

FIG. 9. Maps of the potential temperature, as in Fig. 2, showing the anticyclonic development of the second baroclinic life cycle (initial condition shown in the lower panel of Fig. 1), for 0000 UTC day 11.

phase lines tilt westward; that is, against the winds present there. Its location and relation to the flow are somewhat different from the wave packets discussed in section 3. As seen in Fig. 12, they are found away from the tropopause, with the tilt of their phase lines no longer clearly related to the slope of the tropopause.

The horizontal wavelengths of this wave packet are again found to be of a few hundred kilometers (see Table 3). The vertical wavelength in the reference run ($\Delta x = 50$ km) is comparable to the ones of the lower-stratospheric waves described in section 3a. However, its sensitivity to resolution is different: as for the surface front waves (section 4a), the vertical wavelength is fairly stable relative to resolution. In consequence, their intrinsic frequency increases from $1.4f$ to $2f$ when resolution is increased from moderate to high, and the vertical group velocity correspondingly increases from $(3 \pm 0.5) \times 10^{-2}$ m s^{-1} to $(6.5 \pm 1) \times 10^{-2}$ m s^{-1} (see Fig. 13).

The sensitivity of the vertical wavelength to resolution and the vertical cross sections of Figs. 12 and 13 again suggest, as for the surface front waves, that the generation mechanism could be interpreted in terms of a topographic effect. Note indeed how the height of the isentropes varies above the deep tongue of stratospheric air. Further work is again needed.

5. Phase speed of the excited gravity waves

The purpose of the present section is to highlight a characteristic that all the wave packets identified above share. In horizontal maps at successive times, their phase lines clearly remain attached to a feature of the baroclinic wave. In other words, their phase speed relative to the ground matches that of the baroclinic wave (typically 13–15 m s^{-1}). This is shown most conveniently using Hovmöller diagrams in Fig. 14, where phase lines of the baroclinic and gravity waves are parallel or nearly parallel.

This point, already noted by O'Sullivan and Dunkerton (1995), is worth emphasizing again because of the importance of the phase speed of gravity waves for the parameterizations of these waves in global models (Fritts and Alexander 2003).

6. Discussion

The spontaneous generation of gravity waves in idealized simulations is a numerically sensitive problem and several issues need to be discussed. First, one could fear that these gravity waves are not spontaneously generated but come from the initial condition. Care has been taken here to prepare initial conditions that are as balanced as possible (section 2, appendix A), in order to rule out this possibility. Moreover, preliminary simulations in which the initial conditions were not as cleanly prepared gave the same results. Hence, we are confident that the gravity waves do not come from the initial condition.

Second, inertia–gravity waves and front have scales near the grid resolution in certain regions and that scale decreases with increased resolution and decreased hyperdiffusion. This raises two issues: the possibility that some aspects of the solution are artifacts arising from numerical discretization errors and the dependence of the solutions on the form and magnitude of the explicit dissipation.

Discretization errors associated with insufficient vertical resolution may lead to spurious, numerically generated waves near fronts (e.g., Snyder et al. 1993; Bush et al. 1995). In such cases the frontal surface exhibits distinct corrugations at each grid level and standing

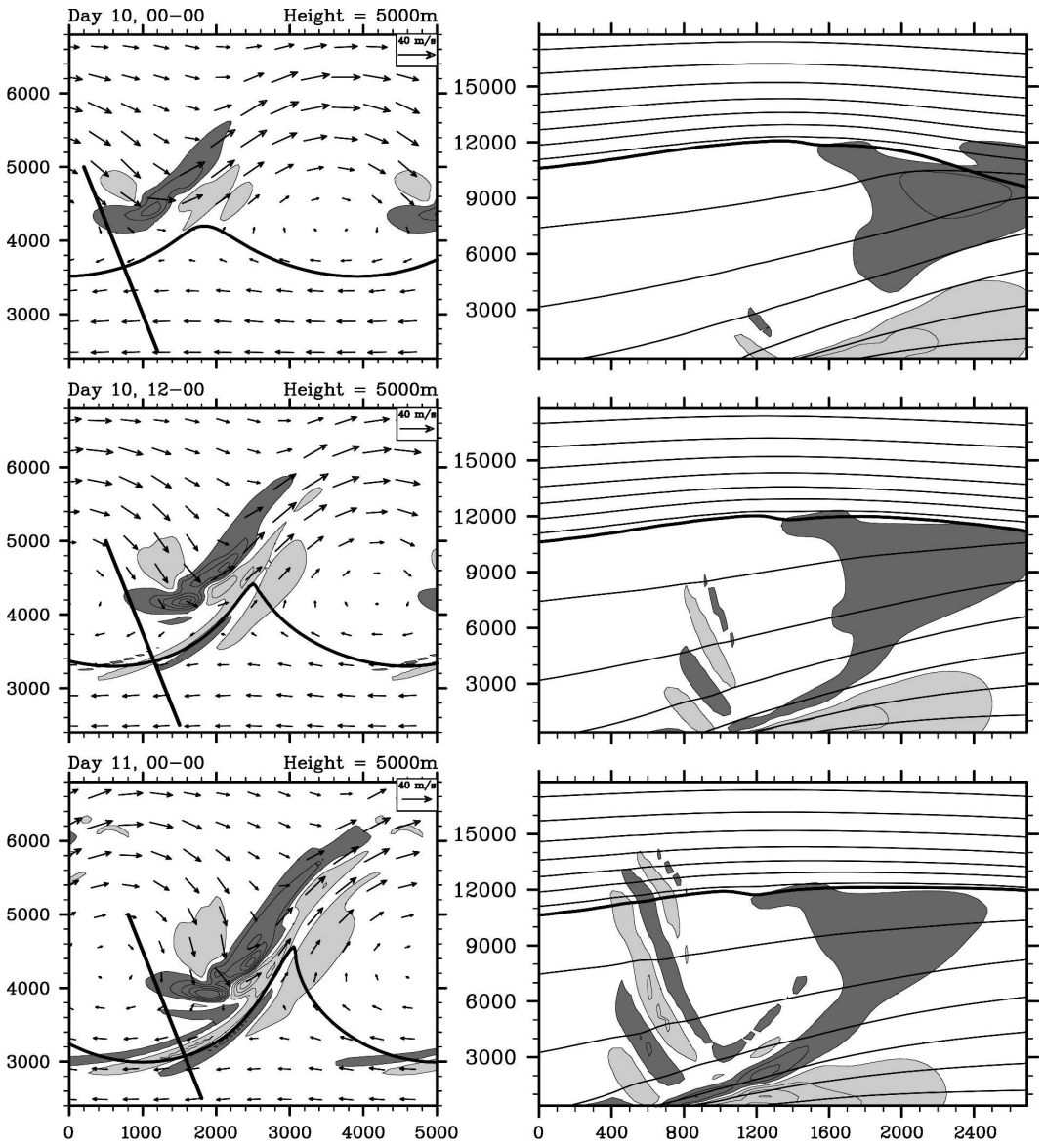

FIG. 10. Inertia–gravity waves appearing in the vicinity of the surface fronts, in the life cycle with added anticyclonic shear. Plots are as in Fig. 3, except that horizontal cross sections of $\nabla \cdot \mathbf{u}_H$ (left column) are shown at $z = 5$ km and include one isentrope (thick line) depicting the surface fronts, and times shown are (top) 0000 UTC day 10, (middle) 1200 UTC day 10, and (bottom) 0000 UTC day 11. As in Fig. 8, the lines in the vertical cross sections at right indicate the potential temperature (every 10 K).

waves trapped between the front and the surface. Avoiding these spurious features requires that the grid aspect ratio dx/dz should be comparable to the frontal slope, of the order of N/f (Snyder et al. 1993; Pecnick and Keyser 1989; Lindzen and Fox-Rabinowitz 1989). In our simulations, N is typically 0.01 s^{-1} in the troposphere and nearly 0.02 s^{-1} in the lower stratosphere, and $f = 10^{-4}$ s^{-1}. The vertical resolution we use ($dz = dx/200$)

TABLE 2. Characteristics of the inertia–gravity waves present in the anticyclonic run above the surface front (section 4a). Column headings are the same as Table 1.

Resolution	λ_x	λ_y	λ_H	λ_z	$\tilde{\omega}$
$\Delta x = 100$ km	915 ± 80	555 ± 40	475 ± 35.	5.45 ± 0.15	1.48 ± 0.05
$\Delta x = 50$ km	715 ± 25	345 ± 25	310 ± 20	5.55 ± 0.1	2.0 ± 0.1
$\Delta x = 25$ km	490 ± 60	230 ± 30	210 ± 25	6.4 ± 0.2	3.0 ± 0.4

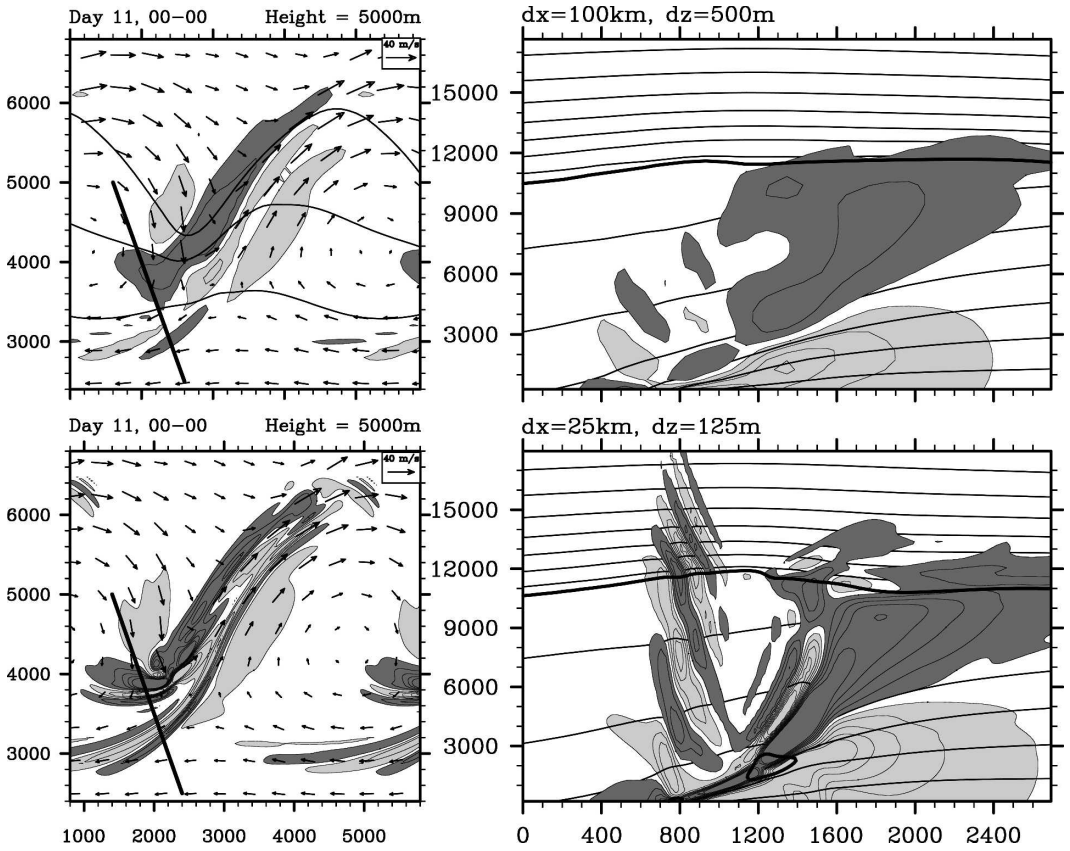

FIG. 11. (left) Horizontal and (right) vertical cross sections to be compared with those of the bottom row in Fig. 10 (anticyclonic life cycle, 0000 UTC day 11). The resolution is (top) halved and (bottom) doubled.

is thus as advised in the lower stratosphere and more than sufficient elsewhere. With this resolution, the solutions exhibit neither the corrugations of the frontal surface nor the standing waves beneath the front that would indicate numerical discretization errors were important. More important, the solutions are not sensitive to changes in the vertical resolution; doubling the vertical resolution hardly changes the results (not shown), which argues strongly against a role for numerical discretization errors. Hence, the authors are also confident that the inertia–gravity waves in the simulations are not numerical artifacts.

At the same time, the solutions presented here clearly depend on the magnitude and form of explicit dissipation in the numerical model. Both the frontal scale and the wavelength of any excited gravity waves decrease rapidly in regions of strong deformation. Without explicit small-scale dissipation in the model, gradients at the grid scale increase until the simulations are obviously contaminated by numerical errors. Explicit dissipation is therefore essential in our simulations. Moreover, we have chosen the dissipation to be large enough to limit the power in near grid-scale features and thus to avoid significant numerical errors.

We have explored the sensitivity of our simulations to the explicit dissipation both by varying the form of the dissipation operator and by employing different resolutions with the explicit hyperdiffusion reduced at higher resolution as described in section 2. Considering first the form of the dissipation, Fig. 15 shows horizontal cross sections of $\nabla \cdot \mathbf{u}_H$ that have been obtained from four simulations of the standard life cycle: without explicit dissipation, with second-order diffusion ($\nu_2 = 1.5 \times 10^4$ m^2 s^{-1}), with fourth-order diffusion ($\nu_4 = 3.75 \times 10^{13}$ m^4 s^{-1}), and with fourth-order diffusion with a variable diffusivity coefficient (see section 2). Although the waves are qualitatively similar across all these simulations, they are sensitive in amplitude to the form of the dissipation, especially where their wavelengths have shrunk and approach the grid scale. We emphasize, however, that this sensitivity does not imply that the dissipation plays a role in the generation of these waves——the waves are affected by dissipation as

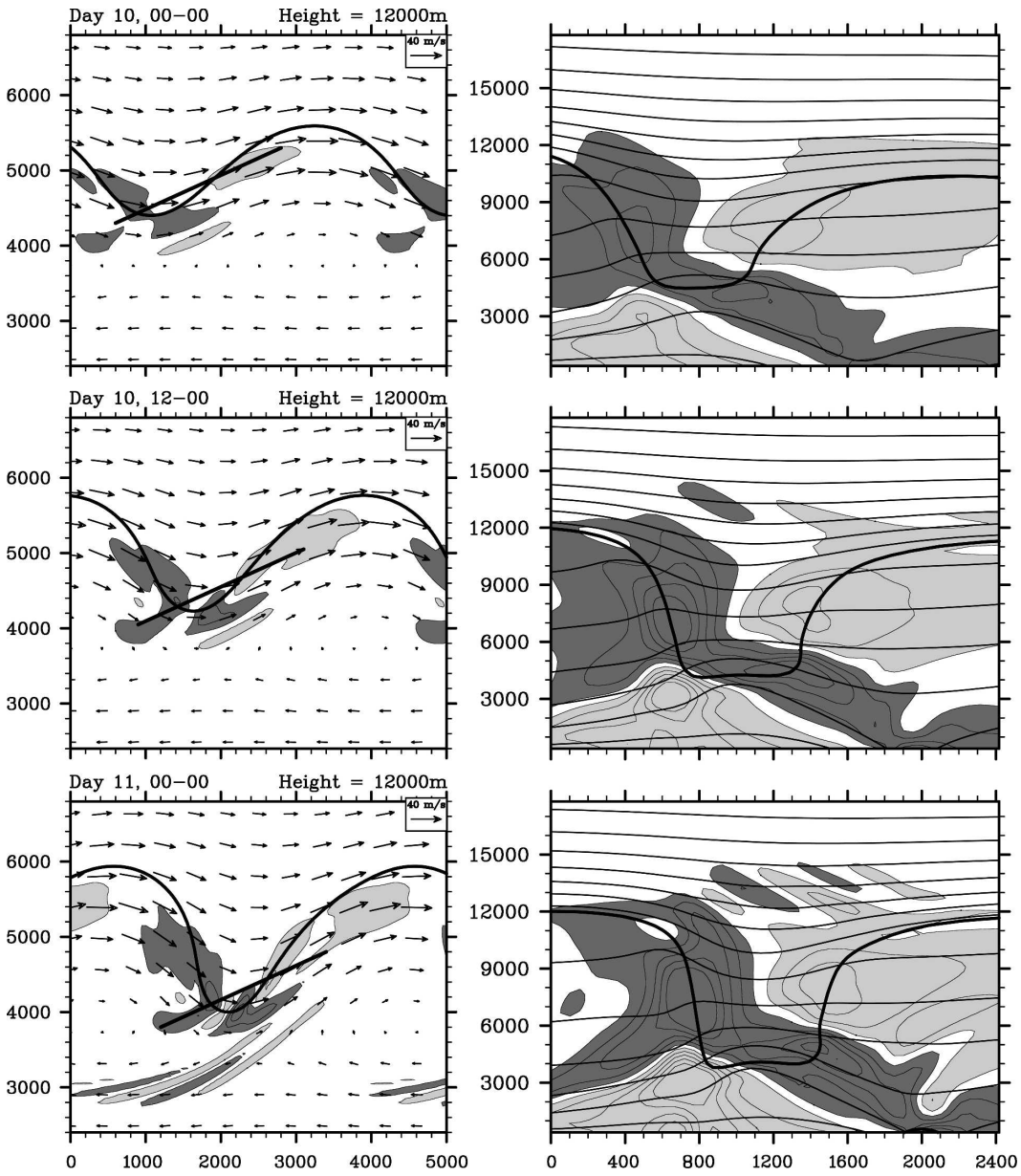

FIG. 12. Second wave packet identified in the anticyclonic run, in the lower stratosphere. The presentation is the same as Figs. 3 and 10. The horizontal cross sections in the left column are made at $z = 12$ km.

are all other small-scale motions, even if they are excited by an inviscid process. Moreover, the waves increase as dissipation decreases, which is strongly suggestive of an inviscid emission.

The waves also change when the dimensional coefficient of the hyperdiffusion changes for higher- or lower-resolution simulations. Recall from section 2 that we choose the maximum hyperdiffusion to scale as dx^4/

TABLE 3. Characteristics of the inertia–gravity waves present in the anticyclonic run in the tropopause region. Column headings are the same as Table 1.

Resolution	λ_x	λ_y	λ_H	λ_z	$\tilde{\omega}$
$\Delta x = 100$ km	585 ± 35	785 ± 60	470 ± 23	2.9 ± 0.25	1.36 ± 0.05
$\Delta x = 50$ km	440 ± 20	550 ± 37	343 ± 18	2.2 ± 0.1	1.38 ± 0.02
$\Delta x = 25$ km	220 ± 17	430 ± 21	195 ± 12	2.3 ± 0.10	2.0 ± 0.1

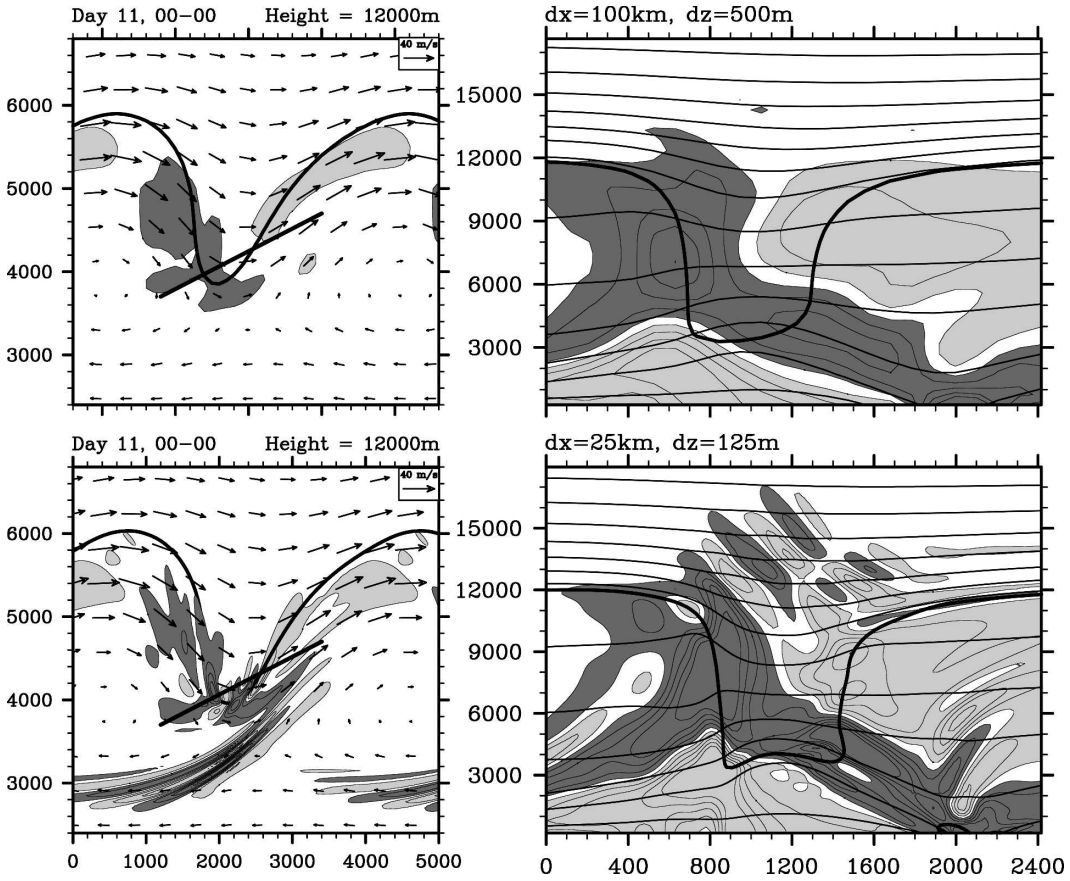

FIG. 13. (left) Horizontal and (right) vertical cross sections to be compared with those of the bottom row in Fig. 12 (anticyclonic life cycle, 0000 UTC day 11). The resolution is (top) halved and (bottom) doubled.

dt, so that doubling resolution (and halving the time step) decreases the hyperdiffusion by a factor of 8. Two sensitivities need to be considered, that of the baroclinic life cycle itself, and that of the inertia–gravity waves.

For the overall development of the baroclinic instability itself, the sensitivity to resolution and dissipation is small: the growth rate changes by a little more than 2% as the resolution is doubled. Details of the baroclinic wave do change as the resolution is increased: the surface fronts, and to a much lesser extent the upper-level front, collapse further when the dissipation is smaller, leading to stronger gradients.[2] When the resolution is doubled, the maximum relative cyclonic vorticity in the surface front roughly doubles, whereas it increases only by about 25% in the upper-level front. This sensitivity of the frontal features to dissipation is well known from previous studies (e.g., Snyder et al. 1993), and is inevitable unless one adds unrealistically high dissipation. It is also worth noting that local Rossby numbers calculated as the ratio of relative to planetary vorticity are comparable in both the cyclonic and anticyclonic simulations (at the standard resolution: 4–5 near the surface fronts, around 1.5 at $z = 9$ km), and hence that these are not a sufficient indicator to diagnose regions of generation of gravity waves.

Regarding the inertia–gravity waves, we will first note that nesting could possibly have been used to obtain additional resolution and lower dissipation. However, this would come at the cost of potential numerical artifacts in the transitions from one domain to another, in particular in sensitive fields such as the vertical velocity and in crucial regions such as the fronts. Hence it was chosen not to use nesting in the present study.

[2] Thus, the frontal scale in our simulations is clearly set by the model's explicit dissipation. It is not clear what process, if any, limits frontal scales the atmosphere. Nevertheless, intense atmospheric fronts form rapidly and frequently, and typically persist for several days. Thus, the process by which the frontal scale equilibrates in our solutions is not realistic but existence and persistence of intense fronts is realistic.

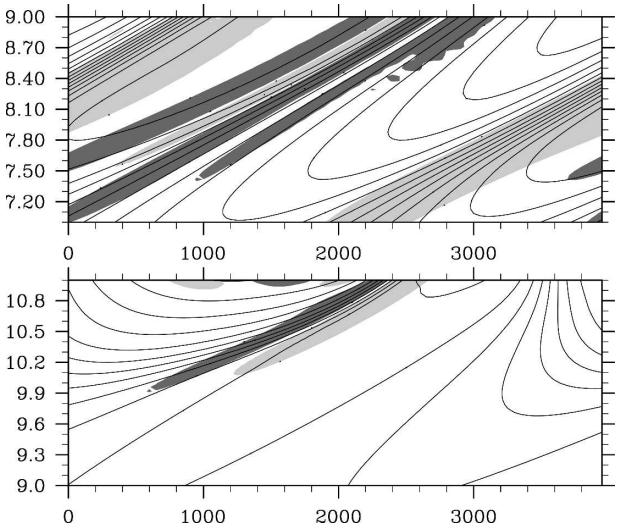

FIG. 14. Hovmöller diagrams showing the propagation of the gravity waves at the same phase speed as the baroclinic waves. Horizontal axis shows x in km, vertical axis is time in days. (upper) $\nabla \cdot \mathbf{u}_H$ (gray shading, as in Fig. 3) and potential temperature for $y = 5000$ km, $z = 11$ km (contours every 5 K) in the standard life cycle (wave packet described in section 3a). (lower) Similarly, $\nabla \cdot \mathbf{u}_H$ for $y = 4300$ km, $z = 2.5$ km, and potential temperature for $y = 4300$ km, $z = 150$ m (contours every 2.5 K) in the anticyclonic life cycle (wave packet described in section 4a).

For the sensitivity of the inertia–gravity waves themselves to dissipation and resolution, several reasons are possible. The waves may change because the source and generated waves change as resolution increases and dissipation decreases, allowing a source with smaller scales to generate waves with smaller scales, or, the source and generated waves being unchanged, because propagation effects lead to finer and finer wavelengths [effect of the shear as in O'Sullivan and Dunkerton (1995), or of deformation as in Plougonven and Snyder (2005)]. This latter effect, due to propagation of waves in a complex flow, is unavoidable, as it is for the advection of a passive tracer leading to finer and finer scales as resolution is increased (Bühler and McIntyre 2005).

Now, for the four wave packets that have been identified in sections 3a, 3b, 4a, and 4b, different sensitivities to resolution need to be distinguished: sensitivity in amplitude and in characteristics (wavelengths, intrinsic frequency).

The waves excited by the upper-level jet (section 3a), show some sensitivity in both characteristics (wavelengths only) and amplitude. The wavelengths within the wave packet are inhomogeneous. As resolution is doubled (Table 1), the minimal wavelength at the front of the wave packet decreases, yet the rest of the cross sections show quite comparable signals (Figs. 3, 6) and the intrinsic frequency is remarkably insensitive to resolution. This suggests that although the simulations do not converge, they are describing correctly a part of the wave dynamics, even at the lowest resolution.[3] Plougonven and Snyder (2005) argued that this can be due to propagation effects (wave capture; Bühler and McIntyre 2005) that are well described even at low resolution.

The Zhang wave packet (section 3b) showed a very important sensitivity for the amplitude of the waves: in the low resolution run, these waves were essentially absent, yet they had significant amplitudes at high resolution (Table 4). Similarly, these waves were also very sensitive to the dissipation. On the other hand, the aspect ratio of the waves was not found to vary significantly as resolution was increased from moderate to high.

For the waves excited by the surface fronts (section 4a), the sensitivity in amplitude is similar to the one found for the main wave packet of the standard run, but the sensitivity in the characteristics is very different. Intrinsic frequency increases as the resolution is increased (see Table 2). Phase lines become steeper and the waves propagate upward more quickly (Fig. 11): as the resolution is increased from $\Delta x = 100$ km to $\Delta x = 50$ km and to $\Delta x = 25$ km, the vertical group velocity goes from 0.15 to 0.25 m s^{-1} and finally to 0.53 m s^{-1}.

Finally, the waves excited above the tip of the tropopause fold in the anticyclonic run exhibit significant sensitivity in both amplitude and characteristics (section 4b). These waves are essentially absent from the low-resolution run, and their intrinsic frequency increases as resolution is increased, though not as significantly as that of the waves excited above the surface cold front.

In summary, the waves excited in the idealized baroclinic life cycles are likely not numerical artifacts. A number of features remain stable as resolution is increased, suggesting that these simulations will provide valuable information to understand the mechanisms generating the waves. On the other hand, the sensitivity to resolution makes it difficult to conclude on the amplitudes that these waves may have in nearly inviscid flows.

7. Conclusions and perspectives

The spontaneous generation of gravity waves from jets and fronts in simulations of idealized baroclinic life

[3] In the same way, the European Centre for Medium-Range Weather Forecasts (ECMWF) analyses contain valid information on underresolved inertia–gravity waves (Plougonven and Teitelbaum 2003).

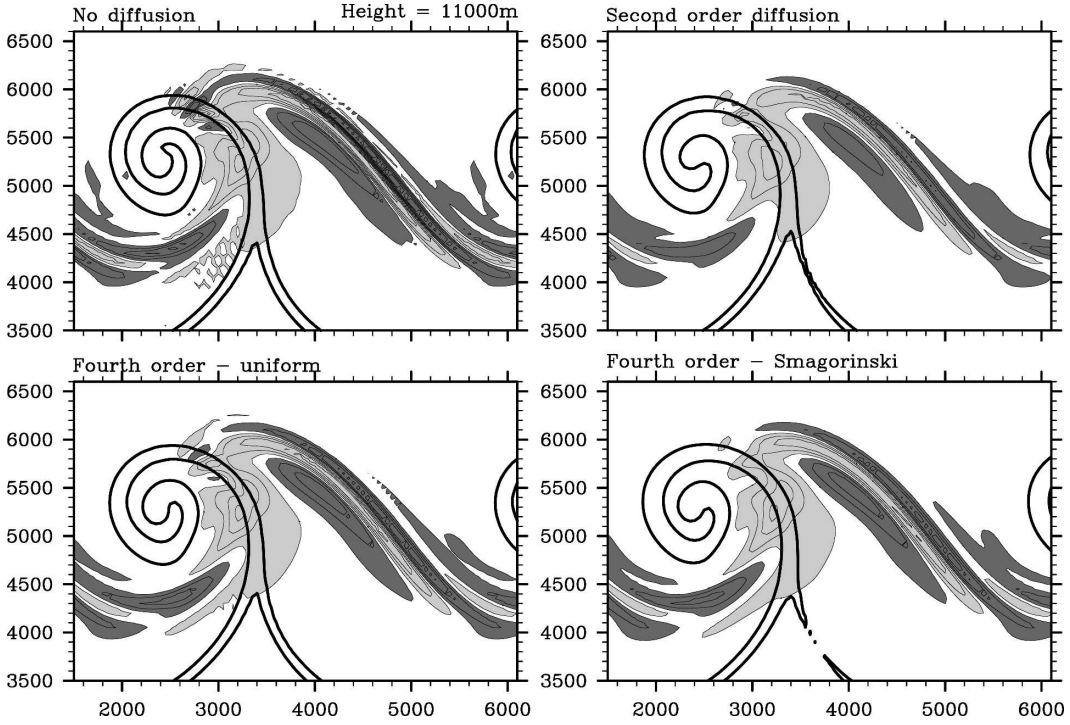

FIG. 15. Horizontal maps of $\nabla \cdot \mathbf{u}_H$ (contours as in Fig. 3) at $z = 11$ km, in simulations of the standard life cycle using different dissipation schemes: (upper left) no explicit diffusion, (upper right) second-order horizontal diffusion, (lower left) fourth order, and (lower right) fourth order with a varying coefficient. As a reminder of the location of the surface front, the contour where the relative vorticity at $z = 150$ m is equal to $1.25f$ is included. In the run without horizontal dissipation, the noisy features that start to appear above the cold front ($x = 3000$ km, $y = 4300$ km) are spurious numerical features that made it necessary to include explicit diffusion.

cycles has been described. The investigation of two very different life cycles showed that the generation can depend strongly on the details of the baroclinic wave's development.

The first baroclinic life cycle was dominated by the development of cyclonic vortices (Fig. 2). The most conspicuous gravity wave packets are found in the highly sheared regions just above and below the jet core, from ridge to trough (Fig. 3). Their upward and downward propagation away from the jet is clear indication that the source of the waves is the jet. The stratospheric waves are similar to the ones described by O'Sullivan and Dunkerton (1995). Their low intrinsic frequency ($\sim 1.3f$), on the other hand, is stable regardless of resolution, which is likely evidence of the importance of propagation effects (Plougonven and Snyder 2005).

Another wave packet was found in this first baroclinic life cycle. It is located in the upper-troposphere and lower stratosphere, above the location of the occlusion at the surface (section 3b), and is very similar to the one described by Zhang (2004). The complex structure of this wave packet and of the flow around and below it make it difficult to determine clear values for its characteristics or to identify tentatively a source.

The second baroclinic life cycle was dominated by

TABLE 4. Order of magnitude for the amplitudes of the divergence associated with the different wave packets. From the standard baroclinic life cycle: main wave packet (section 3a) above the jet (column 1), below the jet 2, Zhang wave packet (3, section 3b), and the surface front waves (4, section 3c). From the anticyclonic life cycle: waves above the cold front (5, section 4a), and waves in the lower stratosphere (6, section 4b).

	1	2	3	4	5	6
$\Delta x = 100$ km	0.05–0.06f	0.04–0.08f	—	—	0.05–0.07f	0.02–0.04f
$\Delta x = 50$ km	0.15–0.2f	0.1–0.14f	0.02–0.04f	0.008–0.012f	0.1–0.15f	0.08–0.12f
$\Delta x = 25$ km	0.25–0.3f	0.15–0.20f	0.1–0.15f	0.015–0.02f	0.25–0.3f	0.15–0.2f

anticyclonic behavior (Fig. 9). The most conspicuous gravity wave packet was found in the troposphere ahead of the cold front (Fig. 10). The waves had higher intrinsic frequencies (1.5–3f; Table 2), and hence larger group velocities. In contrast to the waves in the standard life cycle, their intrinsic frequency was sensitive to resolution (Fig. 11; Table 2) but their vertical wavelength was not. This difference likely indicates that the generation mechanism is different.

A second wave packet was found in this anticyclonic baroclinic life cycle. It is located in the tropopause region, in the trough and just downstream of it (section 4b). In contrast to the lower-stratospheric wave packet described in the standard baroclinic life cycle (section 3a), the waves do not appear confined a region of sharp vertical shear just above the tropopause (see Fig. 12). Moreover, they also differ by the sensitivity of their intrinsic frequency to the resolution.

All these different wave packets share one important feature (section 5): they are nearly stationary with respect to the synoptic-scale baroclinic wave and thus their zonal phase speed relative to the ground is the same as that of the baroclinic wave (13–15 m s^{-1}). This may be of importance to modelers, as the corresponding momentum fluxes will always be in the eastward direction.

We have not emphasized the amplitude of these simulated wave packets as it depends significantly on the dissipation in the numerical model and on resolution, to the extent that we decrease the model's explicit dissipation as resolution increases. The wave amplitude increases as the dissipation decreases (and resolution increases) and the present simulations thus underestimate wave amplitude in these idealized flows. In the real atmosphere, surface drag and mixing in the planetary boundary layer likely have the opposite effect, slowing the development of the baroclinic system and its fronts and reducing wave generation (though not eliminating it; see Fig. 11 of Rotunno et al. 1998).

Overall, the different life cycles emphasize different source regions and possibly different generating mechanisms. This study brings together, in one set of simulations, results from several previous works, and presents a new type of excited wave packet. With the possibility of producing other (intermediate) baroclinic life cycles, this provides a consistent framework that will be used in Part II (in preparation) to pursue the study of the spontaneous generation of gravity waves from balanced flows.

The challenge remains to explain quantitatively this generation. Because of the dependence on dissipation and resolution, previous studies (O'Sullivan and Dunkerton 1995; Zhang 2004) have focused on one case and increased the resolution as much as possible. Our approach is complementary: we have shown that simulations at an intermediate resolution ($\Delta x = 50$ km) already carry valuable and reliable information. Comparison of different simulations at this resolution is underway to test systematically the relevance of different imbalance diagnostics as predictors for inertia–gravity wave generation (Plougonven and Zhang 2007 and references therein), and to discuss the effects of the horizontal propagation, as it was shown that these effects could be important (Plougonven and Snyder 2005).

Acknowledgments. The authors wish to thank Rich Rotunno for discussions and comments on the manuscript, David J. Muraki and Fuqing Zhang for stimulating discussions, and Bill Skamarock, Wei Wang, George Bryan, and Todd Lane for help with the numerical model. RP was supported by an Award for Newly Appointed Lecturers of the Nuffield Foundation, and by the Progamme National de Chimie Atmosphérique. Computing resources were provided by NCAR's Scientific Computing Division. CS acknowledges support from the National Science Foundation through Grant CMG-0327582.

APPENDIX A

Initial Conditions for the Simulations

To have a sharp and well-defined tropopause, we obtain the balanced zonal jet by inverting a specified PV distribution in the (y, z) plane. This distribution is specified in a form similar to that described by Rotunno et al. (1994). In contrast to these authors however, we are not making the Boussinesq approximation. To invert the PV in the primitive equations, we change coordinates to (y, π) coordinates (cf. Davis and Emanuel 1991), where $\pi = c_p(P/P_0)^\kappa$ is the Exner function, with $c_p = 1004$ J K^{-1} kg^{-1}, P_0 a reference pressure value, and $\kappa = 287/1004$. As we consider a purely zonal flow, the geostrophic solution is an exact stationary solution of the full equations. Expressing PV in (y, π) coordinates leads to a single equation for q involving only one variable, Φ, the geopotential height [cf. Davis and Emanuel (1991), their Eq. (2.3)]. This equation is solved by successive overrelaxation, as in Rotunno et al. (1994).

The boundary conditions specified are zero wind on the lateral walls, the potential temperature at the top of the domain in (y, π), and the value of Φ at the bottom of the domain in (y, π). To change the nonlinear development of the baroclinic instability and obtain different life cycles, previous authors have typically added barotropic shear (e.g., Thorncroft et al. 1993). Here, in order to preserve the structure of the PV field, we have

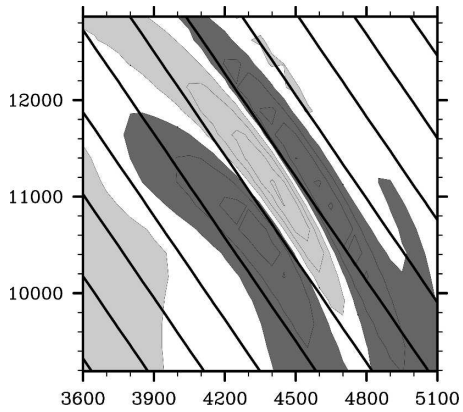

FIG. B1. Zonal cross section comparing the raw divergence field and the spatial wave characteristics obtained as described in appendix B, for the standard run, 1200 UTC day 8. Horizontal axis is x in km, vertical axis is z in m, and the section is taken at y = 5300 km. The black lines show the zero phase lines for a sinusoidal signal with wavelengths λ_x = 475 km, λ_y = 525, and λ_z = 1.7 km.

simply modified the lower boundary condition, specifying Φ on $\pi = c_p$ so as to have constant shear in the center of the domain, and a smoothly vanishing zonal velocity and relative vorticity near the lateral boundaries.

APPENDIX B

Quantifying the Characteristics of the Waves

To identify the wavelengths (λ_x, λ_y, and λ_z), a volume containing the wave packet of interest was isolated for two fields, the divergence and the vertical velocity, either raw or filtered using running averages. For each zonal, meridional, and vertical profile, the wavenumber such that a sinusoidal signal best correlated with the initial field was found. The wavenumbers thus obtained were then averaged and considered robust if two conditions were met: 1) plots confirmed that they described well the wave packet (see, e.g., Fig. B1); 2) the results exhibited only small variations when different filters were used. The method in general is robust, although it may tend to slightly overestimate the wavelengths. In Tables 1–3, the error bars indicated were obtained as the standard deviation of the results obtained from applying the method either to the vertical velocity or to divergence, using different filters or no filter.

REFERENCES

Bosart, L. F., and F. Sanders, 1986: Mesoscale structure in the megalopolitan snowstorm of 11–12 February 1983. Part III: A large-amplitude gravity wave. *J. Atmos. Sci.,* **43,** 924–939.

Bühler, O., and M. E. McIntyre, 2005: Wave capture and wave–vortex duality. *J. Fluid Mech.,* **534,** 67–95.

Bush, A. B., J. C. McWilliams, and W. R. Peltier, 1995: Origins and evolution of imbalance in synoptic-scale baroclinic wave life cycles. *J. Atmos. Sci.,* **52,** 1051–1069.

Buss, S., A. Hertzog, C. Hostettler, T. P. Bui, D. Lüthi, and H. Wernli, 2004: Analysis of a jet stream induced gravity wave associated with an observed ice cloud over Greenland. *Atmos. Chem. Phys.,* **3,** 5875–5918.

Charron, M., and E. Manzini, 2002: Gravity waves from fronts: Parameterization and middle atmosphere response in a general circulation model. *J. Atmos. Sci.,* **59,** 923–941.

Davis, C. A., and K. A. Emanuel, 1991: Potential vorticity diagnostics of cyclogenesis. *Mon. Wea. Rev.,* **119,** 1929–1953.

Eckermann, S. D., and R. A. Vincent, 1993: VHF radar observations of gravity-wave production by cold fronts over Southern Australia. *J. Atmos. Sci.,* **50,** 785–806.

Ford, R., 1994: The response of a rotating ellipse of uniform potential vorticity to gravity wave radiation. *Phys. Fluids,* **6,** 3694–3704.

——, M. E. McIntyre, and W. A. Norton, 2000: Balance and the slow quasimanifold: Some explicit results. *J. Atmos. Sci.,* **57,** 1236–1254.

Fritts, D. C., and Z. Luo, 1992: Gravity wave excitation by geostrophic adjustment of the jet stream. Part I: Two-dimensional forcing. *J. Atmos. Sci.,* **49,** 681–697.

——, and G. D. Nastrom, 1992: Sources of mesoscale variability of gravity waves. Part II: Frontal, convective, and jet stream excitation. *J. Atmos. Sci.,* **49,** 111–127.

——, and M. J. Alexander, 2003: Gravity wave dynamics and effects in the middle atmosphere. *Rev. Geophys.,* **41,** 1003, doi:10.1029/2001RG000106.

Gill, A. E., 1982: *Atmosphere–Ocean Dynamics*. Academic Press, 662 pp.

Griffiths, M., and M. J. Reeder, 1996: Stratospheric inertia–gravity waves generated in a numerical model of frontogenesis. I: Model solutions. *Quart. J. Roy. Meteor. Soc.,* **122,** 1153–1174.

Guest, F. M., M. J. Reeder, C. J. Marks, and D. J. Karoly, 2000: Inertia–gravity waves observed in the lower stratosphere over Macquarie Island. *J. Atmos. Sci.,* **57,** 737–752.

Kim, Y.-J., S. D. Eckermann, and H.-Y. Chun, 2003: An overview of the past, present and future of gravity-wave drag parameterization for numerical climate and weather prediction models. *Atmos.–Ocean,* **41,** 65–98.

Lane, T. P., J. D. Doyle, R. Plougonven, M. A. Shapiro, and R. D. Sharman, 2004: Observations and numerical simulations of inertia–gravity waves and shearing instabilities in the vicinity of a jet stream. *J. Atmos. Sci.,* **61,** 2692–2706.

Lindzen, R. S., and M. Fox-Rabinowitz, 1989: Consistent vertical and horizontal resolution. *Mon. Wea. Rev.,* **117,** 2575–2583.

McLandress, C., and J. F. Scinocca, 2005: The GCM response to current parameterizations of nonorographic gravity wave drag. *J. Atmos. Sci.,* **62,** 2394–2413.

Molemaker, M. J., J. C. McWilliams, and I. Yavneh, 2005: Baroclinic instability and loss of balance. *J. Phys. Oceanogr.,* **35,** 1505–1517.

O'Sullivan, D., and T. J. Dunkerton, 1995: Generation of inertia–gravity waves in a simulated life cycle of baroclinic instability. *J. Atmos. Sci.,* **52,** 3695–3716.

Pavelin, E., J. Whiteway, and G. Vaughan, 2001: Observation of gravity wave generation and breaking in the lowermost stratosphere. *J. Geophys. Res.,* **106** (D6), 5173–5179.

Pecnick, M. J., and D. Keyser, 1989: The effect of spatial resolution on the simulation of upper-tropospheric frontogenesis

using a sigma-coordinate primitive equation model. *Meteor. Atmos. Phys.,* **40,** 137–149.

Plougonven, R., and V. Zeitlin, 2002: Internal gravity wave emission from a pancake vortex: An example of wave–vortex interaction in strongly stratified flows. *Phys. Fluids,* **14,** 1259–1268.

——, and H. Teitelbaum, 2003: Comparison of a large-scale inertia–gravity wave as seen in the ECMWF analyses and from radiosondes. *Geophys. Res. Lett.,* **30,** 1954, doi:10.1029/2003GL017716.

——, and C. Snyder, 2005: Gravity waves excited by jets: Propagation versus generation. *Geophys. Res. Lett.,* **32,** L18892, doi:10.1029/2005GL023730.

——, and V. Zeitlin, 2005: Lagrangian approach to the geostrophic adjustment of frontal anomalies in a stratified fluid. *Geophys. Astrophys. Fluid Dyn.,* **99,** 101–135.

——, and F. Zhang, 2007: On the forcing of inertia–gravity waves by synoptic-scale flows. *J. Atmos. Sci.,* **64,** 1737–1742.

——, H. Teitelbaum, and V. Zeitlin, 2003: Inertia gravity wave generation by the tropospheric midlatitude jet as given by the Fronts and Atlantic Storm-Track Experiment radio soundings. *J. Geophys. Res.,* **108,** 4686, doi:10.1029/2003JD003535.

——, D. J. Muraki, and C. Snyder, 2005: A baroclinic instability that couples balanced motions and gravity waves. *J. Atmos. Sci.,* **62,** 1545–1559.

Polavarapu, S. M., and W. R. Peltier, 1990: The structure and nonlinear evolution of synoptic scale cyclones: Life cycle simulations with a cloud-scale model. *J. Atmos. Sci.,* **47,** 2645–2673.

Ralph, F. M., P. J. Neiman, and T. L. Keller, 1999: Deep-tropospheric gravity waves created by leeside cold fronts. *J. Atmos. Sci.,* **56,** 2986–3009.

Reeder, M. J., and M. Griffiths, 1996: Stratospheric inertia–gravity waves generated in a numerical model of frontogenesis. Part II: Wave sources, generation mechanisms and momentum fluxes. *Quart. J. Roy. Meteor. Soc.,* **122,** 1175–1195.

Reznik, G. M., V. Zeitlin, and M. Ben Jelloul, 2001: Nonlinear theory of geostrophic adjustment. Part 1. Rotating shallow-water model. *J. Fluid Mech.,* **445,** 93–120.

Rotunno, R., C. Snyder, and W. C. Skamarock, 1994: An analysis of frontogenesis in numerical simulations of baroclinic waves. *J. Atmos. Sci.,* **51,** 3373–3398.

——, ——, and ——, 1998: Effects of surface drag on fronts within numerically simulated baroclinic waves. *J. Atmos. Sci.,* **55,** 2119–2129.

Shibata, T., K. Sato, H. Kobayashi, M. Yabuki, and M. Shiobara, 2003: Antarctic polar stratospheric clouds under temperature perturbation by nonorographic inertia gravity waves observed by micropulse lidar at Syowa Station. *J. Geophys. Res.,* **108,** 4105, doi:10.1029/2002JD002713.

Skamarock, W. C., J. B. Klemp, J. Dudhia, D. O. Gill, D. M. Barker, W. Wang, and J. G. Powers, 2005: A description of the Advanced Research WRF Version 2. NCAR Tech. Note NCAR/TN-468+STR, 100 pp.

Snyder, C., W. C. Skamarock, and R. Rotunno, 1991: A comparison of primitive-equation and semigeostrophic simulations of baroclinic waves. *J. Atmos. Sci.,* **48,** 2179–2194.

——, ——, and ——, 1993: Frontal dynamics near and following frontal collapse. *J. Atmos. Sci.,* **50,** 3194–3211.

Stobie, J. G., F. Einaudi, and L. W. Uccellini, 1983: A case study of gravity waves–convective storms interaction: 9 May 1979. *J. Atmos. Sci.,* **40,** 2804–2830.

Thomas, L., R. M. Worthington, and A. J. McDonald, 1999: Inertia–gravity waves in the troposphere and lower stratosphere associated with a jet stream exit region. *Ann. Geophys.,* **17,** 115–121.

Thorncroft, C. D., B. J. Hoskins, and M. E. McIntyre, 1993: Two paradigms of baroclinic-wave life-cycle behaviour. *Quart. J. Roy. Meteor. Soc.,* **119,** 17–55.

Uccellini, L. W., and S. E. Koch, 1987: The synoptic setting and possible energy sources for mesoscale wave disturbances. *Mon. Wea. Rev.,* **115,** 721–729.

Vanneste, J., and I. Yavneh, 2004: Exponentially small inertia–gravity waves and the breakdown of quasigeostrophic balance. *J. Atmos. Sci.,* **61,** 211–223.

Zhang, F., 2004: Generation of mesoscale gravity waves in upper-tropospheric jet–front systems. *J. Atmos. Sci.,* **61,** 440–457.

——, S. E. Koch, C. A. Davis, and M. L. Kaplan, 2001: Wavelet analysis and the governing dynamics of a large amplitude mesoscale gravity wave event along the east coast of the United States. *Quart. J. Roy. Meteor. Soc.,* **127,** 2209–2245.

——, S. Wang, and R. Plougonven, 2004: Uncertainties in using the hodograph method to retrieve gravity wave characteristics from individual soundings. *Geophys. Res. Lett.,* **31,** L11110, doi:10.1029/2004GL019841.